Supplementary Information

Porous $Nb_4W_7O_{31}$ microspheres with a mixed crystal structure for high-performance Li^+ storage

Xingxing Jin[1,#], Qiang Yuan[1,#], Xiaolin Sun[2,3,4,#], Xuehua Liu[1], Jianfei Wu[2,3,4,*], Chunfu Lin[1,*]

[1]Institute of Materials for Energy and Environment, College of Materials Science and Engineering, Qingdao University, Qingdao 266071, Shandong, China.
[2]Qingdao Institute of Bioenergy and Bioprocess Technology, Chinese Academy of Sciences, Qingdao 266101, China.
[3]Shandong Energy Institute, Qingdao 266101, Shandong, China.
[4]Qingdao New Energy Shandong Laboratory, Qingdao 266101, Shandong, China.
[#]Authors contributed equally.

Correspondence to: Prof./Dr. Chunfu Lin, Institute of Materials for Energy and Environment, College of Materials Science and Engineering, Qingdao University, 308 Ningxia Road, Qingdao 266071, Shandong, China. E-mail: linchunfu@qdu.edu.cn; Prof./Dr. Jianfei Wu, Qingdao Institute of Bioenergy and Bioprocess Technology, Chinese Academy of Sciences, 189 Songling Road, Qingdao 266101, Shandong, China; Shandong Energy Institute, 189 Songling Road, Qingdao 266101, Shandong, China; Qingdao New Energy Shandong Laboratory, 189 Songling Road, Qingdao 266101, Shandong, China. E-mail: wujf@qibebt.ac.cn

EXPERIMENTAL

Material preparation

0.86 mmol of ammonium tungstate hydrate ($H_{28}N_6O_{41}W_{12}$, Macklin, 99.99%) and 5.3 mmol of niobium chloride ($NbCl_5$, Macklin, 99.99%) were completely dissolved in 60 mL isopropyl alcohol (IPA). Then, 8 g hexadecyl trimethyl ammonium bromide

(CTMAB, Macklin, 99.99%), 1 mL tetrabutylammonium bromide (TBA, Macklin, 10% in H_2O), and 3 mL hydrochloric acid were slowly added to the above solution with continuous stirring. The resultant homogeneous solution was loaded into a Teflon-lined autoclave (50 mL) and maintained at 180 °C for 24 h. The formed precipitate was separated and washed with distilled water and ethyl alcohol, followed by vacuum drying at 80 °C for 12 h. Finally, the dried precipitate was calcinated at 800 °C for 4 h in air, forming porous $Nb_4W_7O_{31}$ microspheres.

Material characterization

The powder X-ray diffraction (XRD) pattern of $Nb_4W_7O_{31}$ was collected using an X-ray diffractometer (Rigaku Smart Lab) with Cu Kα radiation (λ = 1.5406 Å) at a voltage of 40 kV and a scanning rate of 5° min^{-1}. The *in-situ* XRD experiments were conducted based on an electrochemical cell module equipped with a low-X-ray-absorption Be window (0.2 mm thickness). The lattice constants were obtained by Rietveld refinements of the powder XRD pattern using the free GSAS software with the EXPGUI interface[S1,S2]. The particle size and microstructure were recorded using field emission scanning electron microscopy (FESEM, Hitachi S-4800) equipped with energy-dispersive X-ray spectroscopy (EDX, HORIBA EX-350), and high-resolution transmission electron microscopy (HRTEM, Tecnai G2 F20 and JEM2100). The valence states of the cations were determined by X-ray photoelectron spectroscopy (XPS, Thermo Escalab 250Xi). The nitrogen adsorption–desorption isotherm for calculating the Branauer–Emmett–Teller (BET) specific surface area was recorded on

a surface area analyzer (ASAP 2460). The Barrett–Joyner–Halenda (BJH) model was employed to compute the pore size distribution curve from the desorption branch. The high-angle annular dark field (HAADF) and annular bright field (ABF) scanning transmission electron microscopy (STEM) images were obtained by spherical-aberration-corrected STEM (JEOL JEM-ARM 200F).

Electrochemical test

CR2016-type coin cells were assembled in a glove box filling with pure Ar for evaluating the electrochemical properties of $Nb_4W_7O_{31}$ on an automatic battery testing system (CT-3008, Neware) at ~25 °C. Li metal foils were used as anodes and counter electrodes in the half cells. The working electrodes were fabricated by casting a mixture composed of $Nb_4W_7O_{31}$, Super-P® conductive carbon, and polyvinylidene fluoride (7:2:1 in mass) on Cu current collectors. The electrolyte was composed of 1 M $LiPF_6$ in an ethylene carbonate/diethylene carbonate/dimethyl carbonate mixed solvent (1:1:1 in volume). Celgard® 2325 microporous polypropylene films were employed as separators. The galvanostatic intermittent titration technique (GITT) tests were performed using alternate galvanostatic charge–discharge current pulse at 0.1C for 10 min and rest interval for 20 min. Cyclic voltammograms (CV) were tested on an electrochemical workstation (CHI660E, Chenhua). The electrochemical impedance spectroscope (EIS) experiments were performed on another electrochemical workstation (Interface 1010E, Gamry). All the electrochemical properties of the half cells were examined within 0.8–3.0 V. Furthermore, $LiFePO_4$//$Nb_4W_7O_{31}$ full cells with

a CR2025 coin type were assembled, and their fabrication process is the same as that of the $Nb_4W_7O_{31}$/Li half cells, except for the cathode fabrication. The cathodes were fabricated by casting a mixture composed of $LiFePO_4$ (P198-S21, Shenzhen Kejing Star Technology Co., LTD.), Super-P® conductive carbon, and polyvinylidene fluoride (7:2:1 in mass) on Al current collectors. The electrochemical properties of the full cells were examined within 1.0–2.5 V.

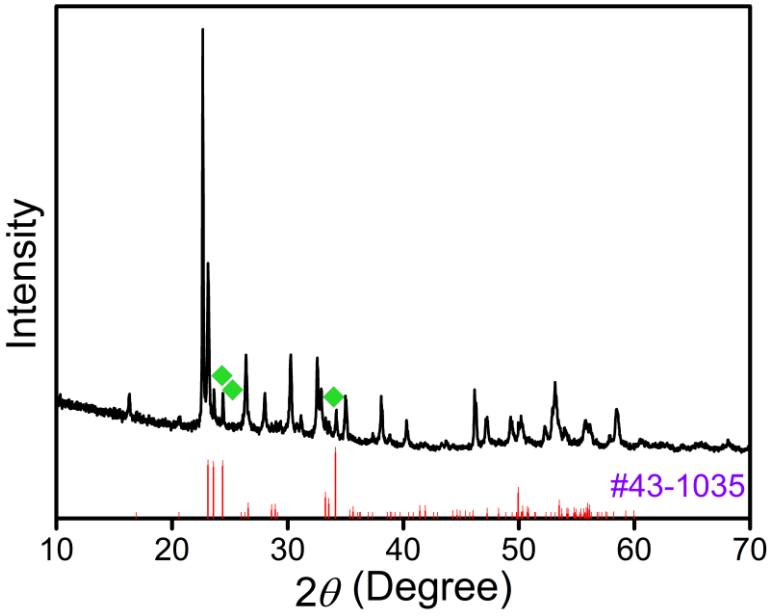

Figure S1. XRD pattern of $Nb_4W_7O_{31}$ containing three obvious peaks of WO_3 (JCPDS 43-1035). ◆: WO_3.

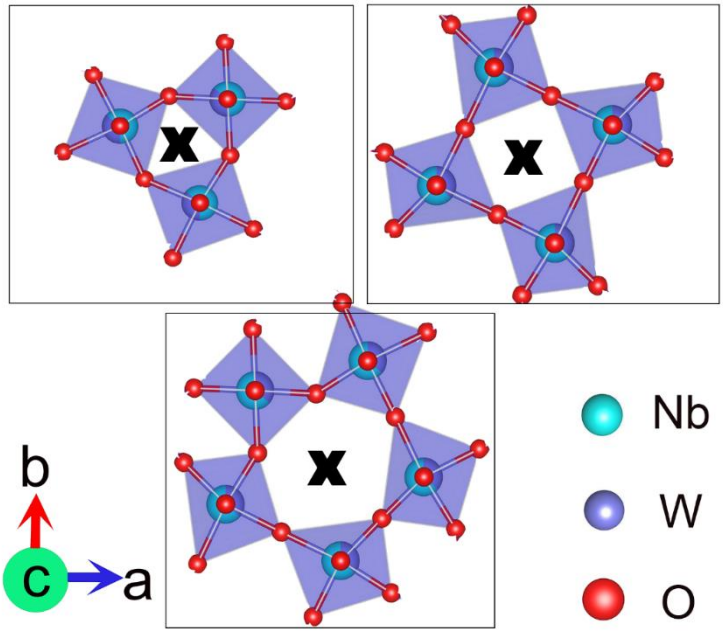

Figure S2. Larger images of three available cavities (pentagonal tunnel, quadrangular tunnel, and triangular tunnel) for possible Li^+-storage in $Nb_4W_7O_{31}$.

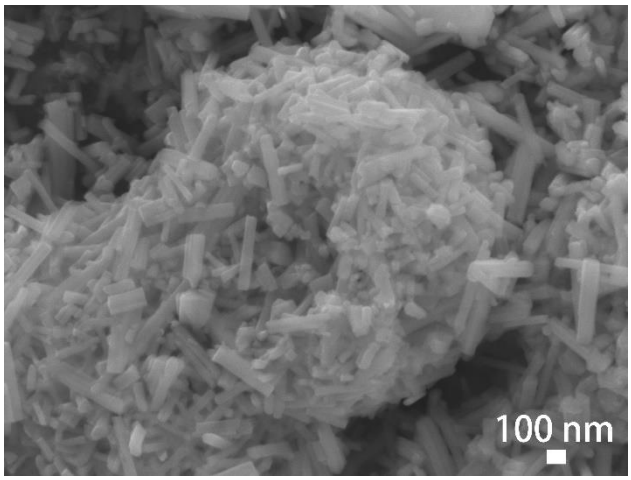

Figure S3. FESEM image of broken $Nb_4W_7O_{31}$ microsphere, showing that the microspheres are not hollow.

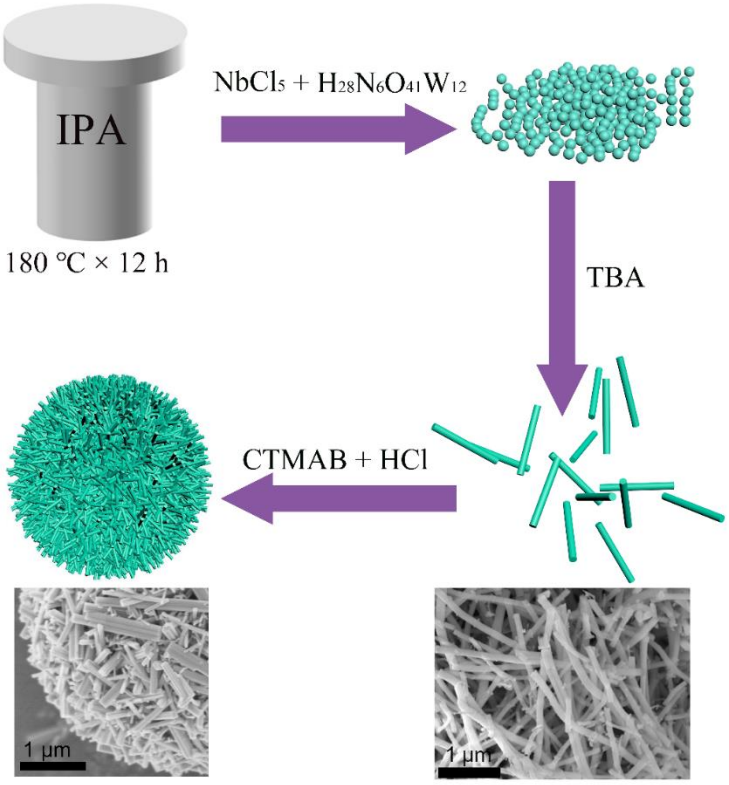

Figure S4. Schematic illustration of solvothermal experiments using different precursors.

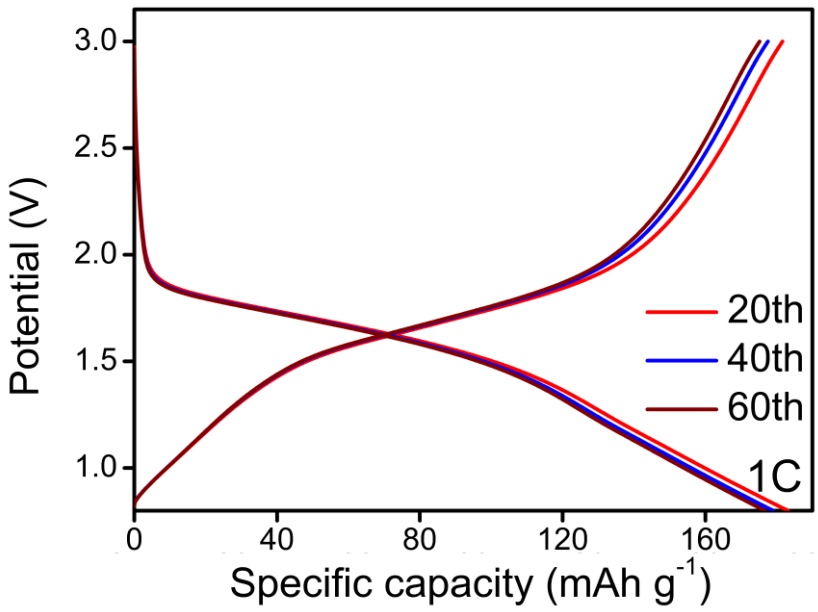

Figure S5. Discharge/charge curves of $Nb_4W_7O_{31}$/Li cell in different cycles at 1C.

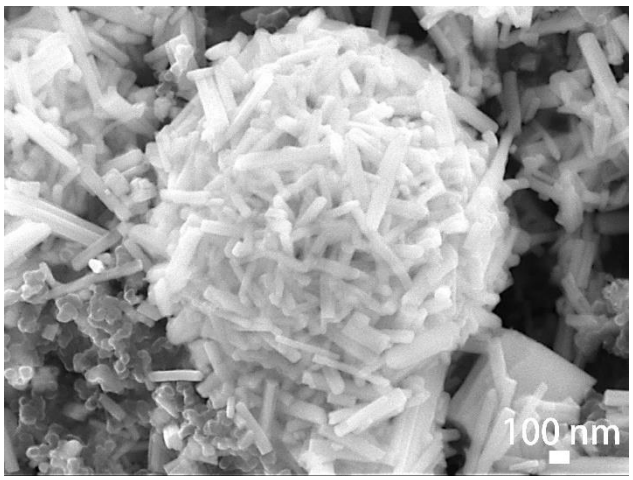

Figure S6. FESEM image of $Nb_4W_7O_{31}$ electrode after 100 cycles at 5C, revealing that porous-microspherical morphology can be retained during the cycling.

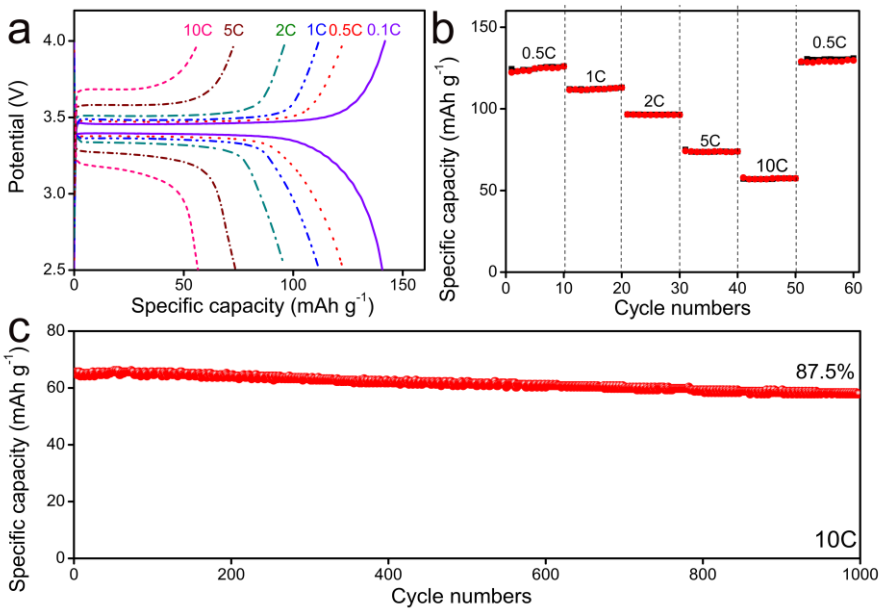

Figure S7. Electrochemical properties of $LiFePO_4$/Li cell (the fabrication process of the $LiFePO_4$/Li cell is the same as that of the $Nb_4W_7O_{31}$/Li cell): (a) charge/discharge curves at various current rates (1C = 170 mA g^{-1}), (b) rate capability, and (c) cyclic stability at 10C over 1000 cycles (after rate-capability test).

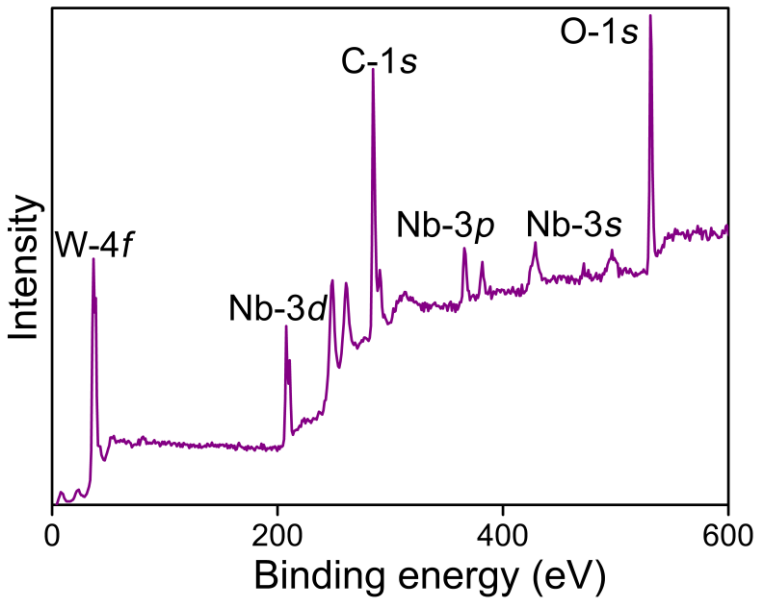

Figure S8. *Ex-situ* XPS spectrum of pristine $Nb_4W_7O_{31}$ sample (OCV).

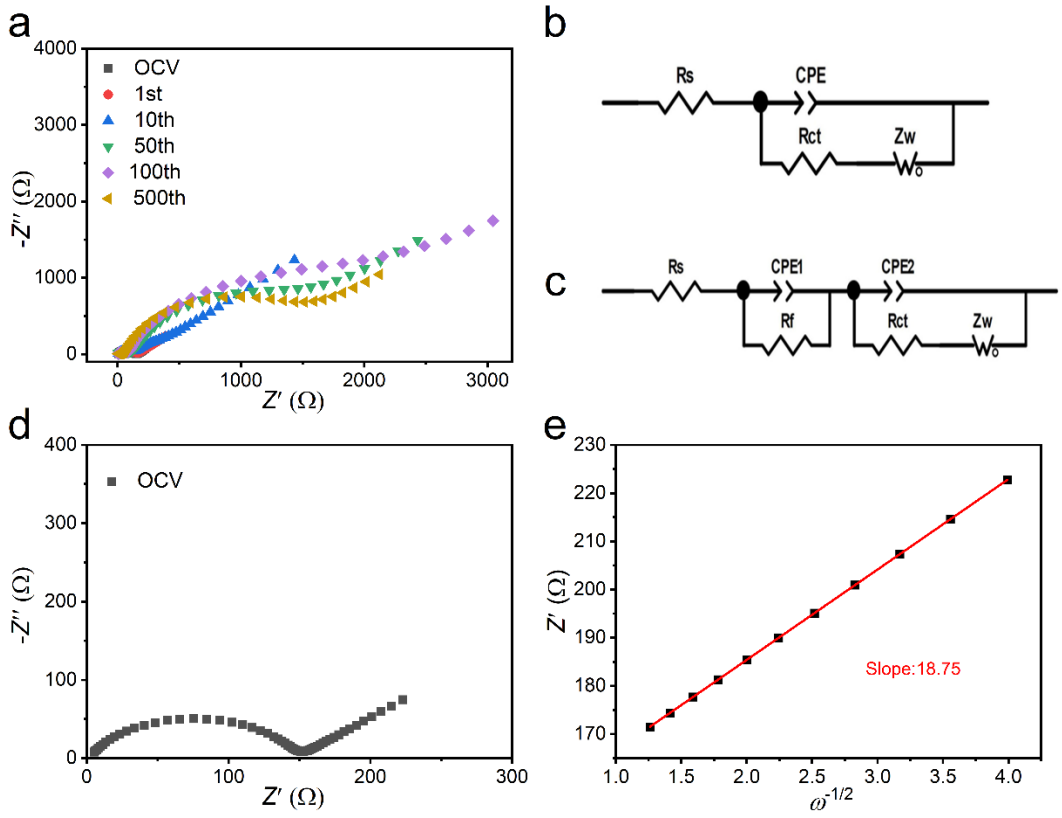

Figure S9. a) Comparison of Nyquist plots of $Nb_4W_7O_{31}$/Li half cell after 0, 1, 10, 50, 100, and 500 cycles. Equivalent circuits for the Nyquist plots b) before first 10 cycles

and c) after 50 cycles. d) Nyquist plot of $Nb_4W_7O_{31}$/Li half cell after 0 cycles (OCV). e) Relationships between Z' and $\omega^{-1/2}$ in low frequency region.

Figure S9a shows the Nyquist plots of the $Nb_4W_7O_{31}$/Li half cell after 0, 1, 10, 50, 100, and 500 cycles at 1C. The equivalent circuit of the plots after 0, 1, and 10 cycles are shown in **Figure S9b**, whereas the plots after 50, 100, and 500 cycles are fitted by the equivalent circuit in **Figure S9c**. R_s relates to the electrolyte resistance of the cell. R_{ct} and Z_w are the charge-transfer and Warburg resistances offered during Li^+ diffusion, respectively. R_f and constant phase elements (CPE or CPE1, CPE2) represent the resistance offered by the electrode surface passive layer and electrode roughness, respectively. As can be seen from **Figure S9a**, the charge-transfer resistance in the high frequency region gradually decreases with the increase of the cycle number, indicating the continuous activation of the $Nb_4W_7O_{31}$ material during the long-term cycling, which can be ascribed to the higher electronic conductivity of the lithiated phase. In addition, after 10 cycles, the semicircle within the high–middle frequency region gradually forms and then keeps stable. Clearly, the solid electrolyte interface (SEI) gradually forms on the particle surface of $Nb_4W_7O_{31}$ and then keeps stable during the long-term cycling.

Moreover, the Nyquist plot in **Figure S9d** at the low-frequency region can be used to calculate the Li^+ ion diffusion coefficient (D_{Li}) using **Equation (S1)** and **(S2)**:[S3]

$$Z_{\text{real}} = R_{\text{ct}} + R_{\text{f}} + \sigma\omega^{-1/2} \quad \text{(S1)}$$

$$D_{\text{Li}} = \frac{R^2T^2}{2A^2n^4F^4{C_{\text{Li}}}^2\sigma^2} \quad \text{(S2)}$$

where R is the gas constant, T is the absolute temperature, A is the surface area of the electrode, n is the transferred electrons number, F is the Faraday's constant, and C_{Li} is the concentration of Li^+ ions in solid. It can be deduced that these values are fixed in the $Nb_4W_7O_{31}$ electrodes, and D_{Li} is directly related to σ. σ is the Warburg factor, which

can be obtained by using the linear relationship between Z_{real} and $\omega^{-1/2}$. As shown in **Figure S9e**, σ of the $Nb_4W_7O_{31}$ electrode is calculated to be 18.75 and the calculated apparent D_{Li} of the $Nb_4W_7O_{31}$ electrode is 1.72×10^{-11} cm^2 s^{-1}.

Table S1. Lattice constants of $Nb_4W_7O_{31}$ with Structure A, Structure B, and Structure C obtained by Rietveld refinements, and their comparisons with those of previously-reported niobate anode compounds. The interlayer spacing (usually equal to the *b* or *c* value) is highlighted in red.

sample	*a* (Å)	*b* (Å)	*c* (Å)	*V* (Å^3)	α, γ (°)	β (°)	reference
$Nb_4W_7O_{31}$-Structure A	**24.557776**	**24.557776**	**3.951166**	**2382.886**	**90**	**90**	**this work**
$Nb_4W_7O_{31}$-Structure B	**24.488878**	**24.488878**	**3.952089**	**2370.088**	**90**	**90**	**this work**
$Nb_4W_7O_{31}$-Structure C	**24.510170**	**24.510170**	**3.952558**	**2374.493**	**90**	**90**	**this work**
$VNb_9O_{24.9}$	15.690	15.690	3.817	939.654	90	90	[S4]
$W_3Nb_{14}O_{44}$	21.02	21.02	3.824	1689.598	90	90	[S5]
$Nb_{18}W_{16}O_{93}$	12.2038	36.6051	3.915	1748.914	90	90	[S6]
$Cu_2Nb_{34}O_{87}$	15.59868	3.83115	20.64336	1135.059	90	113.063	[S7]
$CrNb_{11}O_{29}$	15.6085	3.8335	20.6481	1136.69	90	113.07	[S8]
$FeNb_{11}O_{29}$	28.6862	3.82465	20.6120	2261.43	90	90	[S9]

$TiNb_{24}O_{62}$	29.79212	3.81751	21.09986	2390.526	90	95.018	[S10]
$TiNb_2O_7$	20.36708	3.79885	11.89108	794.945	90	127.227	[S11]
$Cr_{0.5}Nb_{24.5}O_{62}$	29.91514	3.82628	21.15166	2412.092	90	94.944	[S12]
$W_5Nb_{16}O_{55}$	29.657	3.8225	23.106	550.8	90	126.50	[S13]
$WNb_{12}O_{33}$	22.2474	3.8201	17.7290	unrevealed	90	unrevealed	[S14]
$MoNb_{12}O_{33}$	22.27931	3.82094	17.72972	1261.021	90	123.3	[S15]
$ZrNb_{24}O_{62}$	29.87123	3.82209	21.16379	2406.798	90	95.078	[S16]
$AlNb_{11}O_{29}$	15.55789	3.81126	20.53599	1118.354	90	113.303	[S17]
$GaNb_{11}O_{29}$	28.63126	3.80931	20.57555	2244.078	90	90	[S18]
$Mg_2Nb_{34}O_{87}$	15.60459	3.83071	20.64403	1135.119	90	113.096	[S19]
$HfNb_{24}O_{62}$	29.92508	3.82525	21.21133	2418.588	90	95.068	[S20]
$Al_{0.5}Nb_{24.5}O_{62}$	29.9005	3.8228	21.1950	2413.2	90	95.079	[S21]
PNb_9O_{25}	15.615	15.615	3.829	934	90	90	[S22]
$Ti_2Nb_{10}O_{29}$	15.52368	3.81104	20.54768	1118.512	90	113.058	[S23]
$Ti_2Nb_{14}O_{39}$	15.56009	3.82467	20.58537	1125.826	90	113.000	[S24]
$AgNb_{13}O_{33}$	22.3999	3.8337	15.3699	1319.882	90	90	[S25]

$GeNb_{18}O_{47}$	15.7	15.7	3.817	940.85	90	unreaveled	[S26]
$BaNb_{3.6}O_{10}$	17.652	17.482	3.825	1180.46	90	90	[S27]

Table S2. Comparisons of electrochemical properties of $Nb_4W_7O_{31}$ with previously-reported anode materials with intercalation characteristic.

material	rate capability	cyclic stability	reference
$Nb_4W_7O_{31}$ porous microspheres	**120 mAh g^{-1} at 10C**	**capacity retention of 95.2% over 1500 cycles at 10C**	**this work**
$GaNb_{11}O_{29}$ micron-sized particles	121 mAh g^{-1} at 10C	capacity retention of 87.4% over 1000 cycles at 10C	[S18]
$Ti_{0.98}Nb_{2.02}O_7$ micron-sized particles	120 mAh g^{-1} at 10C	capacity retention of 93.3% over 1000 cycles at 10C	[S28]
$TiNb_2O_7$ hierarchical microspheres	100 mAh g^{-1} at 20C	capacity retention of 83.5% over 500 cycles at 10C	[S29]
$Ti_2Nb_{10}O_{29}$ hollow nanofibers	136 mAh g^{-1} at 20C	capacity retention of ~70% over 500 cycles at 10C	[S27]

$Ti_2Nb_{10}O_{29}$ nanofibers	87 mAh g^{-1} at 30C	capacity retention of ~83% over 500 cycles at 10C	[S30]
$Cr_{0.2}Fe_{0.8}Nb_{11}O_{29}$ micron-sized particles	123 mAh g^{-1} at 10C	capacity retention of 86.9% over 500 cycles at 10C	[S31]
$HfNb_{24}O_{62}$ micron-sized particles	78 mAh g^{-1} at 10C	capacity retention of 87.1% over 500 cycles at 10C	[S20]
$TiNb_2O_7$ nanoparticles	76 mAh g^{-1} at 10C	capacity retention of ~84% over 300 cycles at 10C	[S32]
$TiNb_2O_7$ ordered macroporous particles	84 mAh g^{-1} at 20C	capacity retention of ~82% over 1000 cycles at 10C	[S33]
$Li_{3.8}Cu_{0.3}Ti_{4.9}O_{12}$ micron-sized particles	78 mAh g^{-1} at 10C	capacity retention of ~98% over 100 cycles at 10C	[S34]
$BaLi_2Ti_6O_{14}$ micron-sized particles	111.7 mAh g^{-1} at 5C	capacity retention of ~81% over 200 cycles at 10C	[S35]
$W_3Nb_{14}O_{44}$ nanowires	130.6 mAh g^{-1} at 5C	capacity retention of ~64% over 1000 cycles at 10C	[S5]

$Li_4Ti_5O_{12}$ nanorods	135.9 mAh g^{-1} at 10C	capacity retention of 61.5% over 1500 cycles at 10C	[S36]
$Mo_{1.5}W_{1.5}Nb_{14}O_{44}$ micron-sized particles	198 mAh g^{-1} at 10C	capacity retention of 84.1% over 2000 cycles at 10C	[S37]
$Nb_{12}W_{11}O_{63}$ micron-sized particles	100 mAh g^{-1} at 15C	capacity retention of 78.8% over 400 cycles at 0.4C	[S38]
$NiNb_2O_6$ micron-sized particles	126 mAh g^{-1} at 10C	capacity retention of 92.0% over 2500 cycles at 10C	[S39]
$Nb_{14}W_3O_{44}$ nano-blocks	160 mAh g^{-1} at 10C	capacity retention of 84.3% over 1000 cycles at 10C	[S40]
Partially reduced $TiNb_{24}O_{62}$ nanofibers	190 mAh g^{-1} at 10C	capacity retention of 86.4% over 500 cycles at 10C	[S41]
$TiNbO_4$ micron-sized particles	~80 mAh g^{-1} at 10C	capacity retention of ~90.0% over 500 cycles at 1C	[S42]
Reduced $Mo_xTi_{1-x}Nb_2O_{7+y}$ micron-sized particles	192 mAh g^{-1} at 12C	capacity retention of 73.0% over 500 cycles at 12C	[S43]

2D Nb_2O_5-C-rGO micron-sized sheets	~165 mAh g^{-1} at 10C	capacity retention of 78.0% over 1500 cycles at 5C	[S44]
H-Nb_2O_5 with rich Wadsley planar defects micron-sized particles	~160 mAh g^{-1} at 10C	capacity retention of ~86.2% over 2000 cycles at 10C	[S45]
$W_3Nb_{14}O_{44}$ nanowires	~131 mAh g^{-1} at ~3.5C	capacity retention of ~64% over 1000 cycles at ~3.5C	[S5]
$Nb_{18}W_{16}O_{93}$ nanowires	~158 mAh g^{-1} at ~3C	capacity retention of ~59% over 500 cycles at ~6C	[S6]
$W_3Nb_{14}O_{44}$ micron-sized particles	135 mAh g^{-1} at 10C	capacity retention of ~94% over 4000 cycles at 10C	[S46]
$WNb_{60}O_{153}$ nanowires	94 mAh g^{-1} at ~2C	capacity retention of ~75% over 200 cycles at 4C	[S47]
$WNb_{12}O_{33}$ nanowires	146 mAh g^{-1} at 6C	capacity retention of ~86% over 700 cycles at 6C	[S14]
$Nb_{16}W_5O_{93}$ micron-sized particles	148 mAh g^{-1} at 20C*	capacity retention of ~95% over 250 cycles at 10C, followed by 20C with ~95% capacity retention after 750 cycles*	[S13]

$Nb_{18}W_{16}O_{93}$ micron-sized particles	150 mAh g^{-1} at 20C*	capacity retention of ~96% over 250 cycles at 10C, followed by 20C with ~97% capacity retention after 750 cycles*	[S13]

* The current densities of 20C and 10C in Ref. [S13] are equal to that of 10C and 5C in this work.

Table S3. Comparisons of apparent Li^+ diffusion coefficient (D_{Li}) of $Nb_4W_7O_{31}$ with previously-reported M–Nb (V/Ti)–O anode materials.

material	D_{Li} (cm^2 s^{-1})	test technique	reference
$Nb_4W_7O_{31}$ porous microspheres	**6.07×10^{-11}**	**GITT**	**this work**
$Nb_4W_7O_{31}$ porous microspheres	**1.72×10^{-11}**	**EIS**	**this work**
$NiNb_2O_6$ micron-sized particles	1.36×10^{-12}	GITT	[S39]
Partially reduced $TiNb_{24}O_{62}$ nanofibers	8.25×10^{-12}	GITT	[S41]
$TiNb_2O_7$ with predistorted $Nb(Ti)O_6$ octahedrons nanofibers	1.18×10^{-12}	EIS	[S48]
PNb_9O_{25}@CNTs micron-sized particles	4.8×10^{-12}	GITT	[S49]

$W_3Nb_{14}O_{44}$ nanowires	8.02×10^{-13}	CV	[S5]
$Cu_2Nb_{34}O_{87}$ micron-sized particles	3.5×10^{-13}	GITT	[S7]
VNb_9O_{25} nanoribbons	5.17×10^{-15}	EIS	[S50]
$Al_{0.5}Nb_{24.5}O_{62}$ micron-sized particles	2.5×10^{-13}	GITT	[S21]
$MoNb_{12}O_{33}$ micron-sized particles	3.9×10^{-14}	GITT	[S15]
$W_5Nb_{16}O_{55}$ micron-sized particles	1.0×10^{-13}	GITT	[S13]
$GeNb_{18}O_{47}$ nanowires	1.574×10^{-14}	CV	[S26]
$Nb_{18}W_{16}O_{93}$ nanowires	1.312×10^{-14}	EIS	[S6]
$Nb_{12}W_{11}O_{63}$ micron-sized particles	5.10×10^{-15}	EIS	[S38]

$Ru_{0.01}Ti_{0.99}Nb_2O_7$ micron-sized particles	1.66×10^{-15}	EIS	[S51]
$TiNb_2O_7$ nanorods	3.24×10^{-14}	CV	[S52]
$TiCr_{0.5}Nb_{10.5}O_{29}$ nanoparticles	2.07×10^{-14}	CV	[S53]
$Cr_{0.5}Nb_{24.5}O_{62}$ micron-sized particles	4.57×10^{-14}	EIS	[S12]
$Li_{3.08}Cr_{0.02}Si_{0.09}V_{0.9}O_4$ nanowires	1.21×10^{-12}	GITT	[S54]
$HfNb_{24}O_{62}$ micron-sized particles	$1.6\sim1.7\times10^{-12}$	GITT	[S20]
$Fe_{0.4}Ti_{1.6}Nb_{10}O_{28.8}$ micron-sized particles	$\sim3.12\times10^{-12}$	CV	[S55]
$WNb_{60}O_{153}$ nanowires	4.28×10^{-14}	EIS	[S47]
$TiNb_6O_{17}$ micron-sized particles	4.28×10^{-14}	CV	[S56]

5%Cu^{2+}-doped $TiNb_2O_7$ mesoporous microspheres with surface coating of N-doped carbon	3.12×10^{-15}	EIS	[S57]
$Li_4Ti_5O_{12}$ thin films	3.27×10^{-16}	GITT	[S58]
Nb_2O_5 nanorods	3.66×10^{-17}	CV	[S59]
$Mo_{1.5}W_{1.5}Nb_{14}O_{44}$ micron-sized particles	2.01×10^{-17}	GITT	[S37]
TiO_2/C composite nanospheres	2.2×10^{-15}	CV	[S60]

Table S4. Variations in lattice constants of $Nb_4W_7O_{31}$ during first discharge at 0.3C.

point	*a* (*b*)	*c*	*V*
1	24.28509	3.92006	2311.91703
2	24.31973	3.91252	2314.05840
3	24.40631	3.88164	2312.17116
4	24.41456	3.87992	2312.70682
5	24.54980	3.85223	2321.70913
6	24.67844	3.85059	2345.10788
7	24.69493	3.85723	2352.29131
8	24.72709	3.86282	2361.83810
9	24.73534	3.87591	2371.42399

10	24.74358	3.87666	2373.46771
11	24.71060	3.87090	2363.62180
12	24.67844	3.87735	2361.40598
13	24.66194	3.88831	2364.91565
14	24.66194	3.89318	2367.87462
15	24.67844	3.90234	2376.62064
16	24.68668	3.91042	2383.13504
17	24.69493	3.90872	2383.68927
18	24.71060	3.92053	2393.92864
19	24.71060	3.92580	2397.14585
20	24.74358	3.93158	2407.08965
21	24.76750	3.93152	2411.70729
22	24.77574	3.93753	2417.00571
23	24.79223	3.94183	2422.86710
24	24.81697	3.94934	2432.32924
25	24.83347	3.95188	2437.12898
26	24.86563	3.95466	2445.16637
27	24.88212	3.96426	2454.35177
28	24.90686	3.97178	2463.90039
29	24.92335	3.97892	2471.60200
30	24.96458	3.97554	2477.67760
31	24.99014	3.98041	2485.79639
32	25.00664	3.98472	2491.77084
33	25.03962	3.98062	2495.78218

34	25.06436	3.98320	2502.33507
35	25.10641	3.98218	2510.09397
36	25.13198	3.99266	2521.83068
37	25.15672	4.00052	2531.76961
38	25.19053	4.00683	2542.58650
39	25.22434	4.00505	2548.28446
40	25.24990	4.01309	2558.57294
41	25.27546	4.01831	2567.09127
42	25.28371	4.02433	2572.61956
42	25.30103	4.02882	2579.01475

Table S5. Comparisons of volume expansion of $Nb_4W_7O_{31}$ (lithiation) with graphite and previously-reported M–Nb–O anode compounds with shear ReO_3 crystal structures. The interlayer spacing (usually equal to the *b* or *c* value) is highlighted in red.

material	volume expansion (%)	*a* change (%)	*b* change (%)	*c* change (%)	reference
$Nb_4W_7O_{31}$	**11.2**	**4.1**	**4.1**	**2.7**	**this work**
graphite	13.2	little	little	10.2	[S61]
$Mo_3Nb_{14}O_{44}$	10.6	little	little	9.9	[S62]
$Al_{0.5}Nb_{24.5}O_{62}$	8.5	–1.1	10.1	–1.9	[S21]
$FeNb_{11}O_{29}$	6.92	–1.1	6.8	0.4	[S9]

$TiNb_2O_7$	7.22	little	7.89	little	[S11]
$MoNb_{12}O_{33}$	7.80	little	10.0	little	[S15]
$TiNb_{24}O_{62}$	17.5	5.1	9.0	2.9	[S63]
VNb_9O_{25}	8.91	–1.2	–1.2	11.5	[S64]
$Cu_2Nb_{34}O_{87}$	8.32	little	8.34	little	[S7]
$Zn_2Nb_{34}O_{87}$ (orthorhombic)	8.50	little	9.28	little	[S65]
$Zn_2Nb_{34}O_{87}$ (monoclinic)	8.02	little	8.58	little	[S65]

References

[S1] B.H. Toby, EXPGUI, A graphical user interface for GSAS. J. Appl. Crystallogr. 34 (2001) 210–213. [DOI:10.1107/S0021889801002242]

[S2] A.C. Larson, R.B. Von Dreele, General structure analysis system (GSAS), Los Alamos National Laboratory Report LAUR 86-748, 1994.

[S3] T.F. Yi, Y. Xie, Q. Wu, H. Liu, L. Jiang, M. Ye, R. Zhu, High rate cycling performance of lanthanum-modified $Li_4Ti_5O_{12}$ anode materials for lithium-ion batteries, J. Power Sources. 214 (2012) 220–226. [DOI: 10.1016/j.jpowsour.2012.04.101]

[S4] G. Li, X. Wang, X. Ma, Tetragonal $VNb_9O_{24.9}$-based nanorods: a novel form of lithium battery anode with superior cyclability. J. Mater. Chem. A 1 (2013) 12409–12412. [DOI: 10.1039/c3ta12471a]

[S5] L. Yan, J. Shu, C. Li, X. Cheng, H. Zhu, H. Yu, C. Zhang, Y. Zheng, Y. Xie, Z. Guo, $W_3Nb_{14}O_{44}$ nanowires: ultrastable lithium storage anode materials for advanced rechargeable batteries. Energy Storage Mater. 16 (2019) 535–544. [DOI: 10.1016/j.ensm.2018.09.008]

[S6] W. Ye, H. Yu, X. Cheng, H. Zhu, R. Zheng, T. Liu, N. Long, M. Shui, J. Shu, Highly efficient lithium container based on non-Wadsley-Roth structure $Nb_{18}W_{16}O_{93}$ nanowires for electrochemical energy storage. Electrochim. Acta 292 (2018) 331–338. [DOI: 10.1016/j.electacta.2018.09.169]

[S7] L. Yang, X. Zhu, X. Li, X. Zhao, K. Pei, W. You, X. Li, Y. Chen, C. Lin, R. Che, Conductive copper niobate: superior Li^+-storage capability and novel Li^+-transport mechanism. Adv. Energy Mater. 9 (2019) 1902174. [DOI: 10.1002/aenm.201902174]

[S8] Q. Fu, X. Liu, J. Hou, Y. Pu, C. Lin, L. Yang, X. Zhu, L. Hu, S. Lin, L. Luo, Y. Chen, Highly conductive $CrNb_{11}O_{29}$ nanorods for use in high-energy, safe, fast-charging and stable lithium-ion batteries. J. Power Sources 397 (2018) 231–239. [DOI: 10.1016/j.jpowsour.2018.07.020]

[S9] X. Lou, Z. Xu, Z. Luo, C. Lin, C. Yang, H. Zhao, P. Zheng, J. Li, N. Wang, Y. Chen, H. Wu, Exploration of $Cr_{0.2}Fe_{0.8}Nb_{11}O_{29}$ as an advanced anode material for lithium-ion batteries of electric vehicles. Electrochim. Acta 245 (2017) 482–488. [DOI: 10.1016/j.electacta.2017.05.168]

[S10] C. Yang, S. Deng, C. Lin, S. Lin, Y. Chen, J. Li, H. Wu, Porous $TiNb_{24}O_{62}$ microspheres as high-performance anode materials for lithium-ion batteries of electric vehicles. Nanoscale 8 (2016) 18792–18799. [DOI: 10.1039/c6nr04992c]

[S11] C. Yang, C. Lin, S. Lin, Y. Chen, J. Li, $Cu_{0.02}Ti_{0.94}Nb_{2.04}O_7$: an advanced anode material for lithium-ion batteries of electric vehicles. J. Power Sources 328 (2016) 336–344. [DOI: 10.1016/j.jpowsour.2016.08.027]

[S12] C. Yang, S. Yu, C. Lin, F. Lv, S. Wu, Y. Yang, W. Wang, Z. Zhu, J. Li, N. Wang, S. Guo, $Cr_{0.5}Nb_{24.5}O_{62}$ nanowires with high electronic conductivity for high-rate and long-life lithium-ion storage. ACS Nano 11 (2017) 4217–4224. [DOI: 10.1021/acsnano.7b01163]

[S13] K.J. Griffith, K.M. Wiaderek, G. Cibin, L.E. Marbella, C.P. Grey, Niobium tungsten oxides for high-rate lithium-ion energy storage. Nature 559 (2018) 556–563. [DOI: 10.1038/s41586-018-0347-0]

[S14] L. Yan, H. Lan, H. Yu, S. Qian, X. Cheng, N. Long, R. Zhang, M. Shui, J. Shu, Electrospun $WNb_{12}O_{33}$ nanowires: superior lithium storage capability and their working mechanism. J. Mater. Chem. A 5 (2017) 8972–8980. [DOI: 10.1039/c7ta01784g]

[S15] X. Zhu, J. Xu, Y. Luo, Q. Fu, G. Liang, L. Luo, Y. Chen, C. Lin, X. Zhao, $MoNb_{12}O_{33}$ as a new anode material for high-capacity, safe, rapid and durable Li^+ storage: structural characteristics, electrochemical properties and working mechanisms. J. Mater. Chem. A 7 (2019) 6522–6532. [DOI: 10.1039/c9ta00309f]

[S16] C. Yang, Y. Zhang, F. Lv, C. Lin, Y. Liu, K. Wang, J. Feng, X. Wang, Y. Chen, J. Li, S. Guo, Porous $ZrNb_{24}O_{62}$ nanowires with pseudocapacitive behavior achieve high-performance lithium-ion storage. J. Mater. Chem. A 5 (2017) 22297–22304. [DOI: 10.1039/c7ta07347j]

[S17] X. Lou, R. Li, X. Zhu, L. Luo, Y. Chen, C. Lin, H. Li, X. Zhao, New anode material for lithium-ion batteries: aluminum niobate ($AlNb_{11}O_{29}$). ACS Appl. Mater. Interfaces 11 (2019) 6089–6096. [DOI: 10.1021/acsami.8b20246]

[S18] X. Lou, Q. Fu, J. Xu, X. Liu, C. Lin, J. Han, Y. Luo, Y. Chen, X. Fan, J. Li, $GaNb_{11}O_{29}$ nanowebs as high-performance anode materials for lithium-ion batteries. ACS Appl. Nano Mater. 1 (2018) 183–190. [DOI: 10.1021/acsanm.7b00091]

[S19] X. Zhu, Q. Fu, L. Tang, C. Lin, J. Xu, G. Liang, R. Li, L. Luo, Y. Chen, $Mg_2Nb_{34}O_{87}$ porous microspheres for use in high-energy, safe, fast-charging, and stable lithium-ion batteries. ACS Appl. Mater. Interfaces 10 (2018) 23711–23720. [DOI: 10.1021/acsami.8b03997]

[S20] Q. Fu, H. Cao, G. Liang, L. Luo, Y. Chen, V. Murugadoss, S. Wu, T. Ding, C. Lin, Z. Guo, A highly Li^+-conductive $HfNb_{24}O_{62}$ anode material for superior Li^+ storage. Chem. Commun. 56 (2020) 619–622. [DOI: 10.1039/c9cc07447c]

[S21] Q. Fu, R. Li, X. Zhu, G. Liang, L. Luo, Y. Chen, C. Lin, X. Zhao, Design, synthesis and lithium-ion storage capability of $Al_{0.5}Nb_{24.5}O_{62}$. J. Mater. Chem. A 7 (2019) 19862–19871. [DOI: 10.1039/c9ta04644e]

[S22] S. Patoux, M. Dolle, G. Rousse, C. Masquelier, A reversible lithium intercalation process in a ReO_3 – Type structure PNb_9O_{25}. J. Electrochem. Soc. 149 (2002) A391. [DOI 10.1149/1.1455647]

[S23] Q. Fu, J. Hou, R. Lu, C. Lin, Y. Ma, J. Li, Y. Chen, Electrospun $Ti_2Nb_{10}O_{29}$ hollow nanofibers as high-performance anode materials for lithium-ion batteries. Mater. Lett. 214 (2018) 60–63. [DOI: 10.1016/j.matlet.2017.11.076]

[S24] C. Lin, S. Deng, D.J. Kautz, Z. Xu, T. Liu, J. Li, N. Wang, F. Lin, Intercalating $Ti_2Nb_{14}O_{39}$ anode materials for fast-charging, high-capacity and safe lithium-ion batteries. Small 13 (2017) 1702903. [DOI: 10.1002/smll.201702903]

[S25] Z. Chen, X. Cheng, W. Ye, R. Zheng, H. Zhu, H. Yu, N. Long, M. Shui, J. Shu, $AgNb_{13}O_{33}$: a new anode material with high energy storage performance. Chem. Eng. J. 366 (2019) 246–253. [DOI: 10.1016/j.cej.2019.02.091]

[S26] F. Ran, X. Cheng, H. Yu, R. Zheng, T. Liu, X. Li, N. Ren, M. Shui, J. Shu, Nano-structured $GeNb_{18}O_{47}$ as novel anode host with superior lithium storage performance. Electrochim. Acta 282 (2018) 634–641. [DOI: 10.1016/j.electacta.2018.06.109]

[S27] X. Cheng, S. Qian, H. Yua, H. Zhua, Y. Xie, R. Zheng, T. Liu, M. Shui, J. Shu, $BaNb_{3.6}O_{10}$ nanowires with superior electrochemical performance towards ultrafast and highly stable lithium storage. Energy Storage Mater. 16 (2019) 400–410. [DOI: 10.1016/j.ensm.2018.06.018]

[S28] J. Gao, X. Cheng, S. Lou, Y. Ma, P. Zuo, C. Du, Y. Gao, G. Yin, Self-doping $Ti_{1-x}Nb_{2+x}O_7$ anode material for lithium-ion battery and its electrochemical performance. J. Alloy. Compd. 728 (2017) 534–540. [DOI: 10.1016/j.jallcom.2017.09.045]

[S29] H. Li, L. Shen, G. Pang, S. Fang, H. Luo, K. Yang, X. Zhang, $TiNb_2O_7$ nanoparticles assembled into hierarchical microspheres as high-rate capability and long-cycle-life anode materials for lithium ion batteries. Nanoscale 7 (2015) 619–624. [DOI: 10.1039/c4nr04847d]

[S30] D. Pham-Cong, J. Kim, V. Tran, S. Kim, S. Jeong, J. Choi, C. Cho, Electrochemical behavior of interconnected $Ti_2Nb_{10}O_{29}$ nanoparticles for high-power Li-ion battery anodes. Electrochim. Acta 236 (2017) 451–459. [DOI: 10.1016/j.electacta.2017.03.203]

[S31] X. Lou, Z. Xu, Z. Luo, C. Lin, C. Yang, H. Zhao, P. Zheng, J. Li, N. Wang, Y. Chen, H. Wu, Exploration of $Cr_{0.2}Fe_{0.8}Nb_{11}O_{29}$ as an advanced anode material for lithium-ion batteries of electric vehicles. Electrochim. Acta 245 (2017) 482–488.

[DOI: 10.1016/j.electacta.2017.05.168]
[S32] L. Fei, Y. Xu, X. Wu, Y. Li, P. Xie, S. Deng, S. Smirnov, H. Luo, SBA-15 Confined synthesis of $TiNb_2O_7$ nanoparticles for lithium-ion batteries. Nanoscale 5 (2013) 11102–11107. [DOI: 10.1039/c3nr03594h]
[S33] S. Lou, X. Cheng, Y. Zhao, A. Lushington, J. Gao, Q. Li, P. Zuo, B. Wang, Y. Gao, Y. Ma, C. Du, G. Yin, X. Sun, Superior performance of ordered macroporous $TiNb_2O_7$ anodes for lithium ion batteries: understanding from the structural and pseudocapacitive insights on achieving high rate capability. Nano Energy 34 (2017) 15–25. [DOI: 10.1016/j.nanoen.2017.01.058]
[S34] C. Lin, B. Ding, Y. Xin, F. Cheng, M. Lai, L. Lu, H. Zhou, Advanced electrochemical performance of $Li_4Ti_5O_{12}$-based materials for lithium-ion battery: synergistic effect of doping and compositing. J. Power Sources 248 (2014) 1034–1041. [DOI: 10.1016/j.jpowsour.2013.09.120]
[S35] X. Lin, S. Qian, H. Yu, L. Yan, P. Li, Y. Wu, N. Long, M. Shui, J. Shu, Advanced $BaLi_2Ti_6O_{14}$ anode fabricated via lithium site substitution by magnesium. ACS Sustain. Chem. Eng. 9 (2016) 4859–4867. [DOI: 10.1021/acssuschemeng.6b01137]
[S36] L. Xi, H. Wang, S. Yang, R. Ma, Z. Lu, C. Cao, K. Leung, J. Deng, A. Rogach, C. Chung, Single-crystalline $Li_4Ti_5O_{12}$ nanorods and their application in high-rate capability $Li_4Ti_5O_{12}/LiMn_2O_4$ full cells. J. Power Sources 242 (2013) 222–229. [DOI: 10.1016/j.jpowsour.2013.04.020]
[S37] R. Tao, T. Zhang, S. Tan, C. Jafta, C. Li, Liang, X. Sun, T. Wang, J. Fan, Z. Lu, C. Bridges, X. Suo, C. Do-Thanh, S. Dai, Insight into the fast-rechargeability of a novel $Mo_{1.5}W_{1.5}Nb_{14}O_{44}$ anode material for high-performance lithium-ion batteries. Adv. Energy Mater. 12 (2022) 2200519. [DOI: 10.1002/aenm.202200519]
[S38] SX. Ma, L. Cheng, L. Li, X. Cao, Y. Ye, Y. Wei, Y. Wu, M. Sha, Z. Zi, J. Dai, Influence of cut-off voltage on the lithium storage performance of $Nb_{12}W_{11}O_{63}$ anode. Electrochimica Acta 332 (2020) 135380. [DOI: 10.1016/j.electacta.2019.135380]
[S39] R. Xia, K. Zhao, Y. Kuo, L. Zhang, D. M. Cunha, Y. Wang, S. Huang, J. Zheng, B. Boukamp, P. Kaghazchi, C. Sun, J. E. ten Elshof, M. Huijben, Nickel niobate anodes for high rate lithium-ion batteries. Adv. Energy Mater. 12 (2021) 2102972. [DOI: 10.1002/aenm.202102972]
[S40] C. Guo, Z. Liu, K. Han, L. Zhang, X. Ding, X. Wang, L. Mai, Nano-sized niobium tungsten oxide anode for advanced fast-charge lithium-ion batteries. Small 18 (2022) 2107365. [DOI:10.1002/smll.202107365]
[S41] T. Jiang, S. Ma, J. Deng, T. Yuan, C. Lin, M. Liu, Partially reduced titanium niobium oxide: A high-performance lithium-storage material in a broad temperature range. Adv. Sci. 9 (2021) 2105119. [DOI:10.1002/advs.202105119]
[S42] J. Lee, H. Kwak, S. Bak, J. Lee, T. Hong, A. Abbas, H. Bang, New class of titanium niobium oxide for a Li-ion host: $TiNbO_4$ with purely single-phase lithium intercalation. Chem. Mater. 4 (2022) 854–863. [DOI:10.1021/acs.chemmater.1c03960]
[S43] L. Zhao, S. Wang, Y. Dong, W. Quan, F. Han, Y. Huang, Y. Li, X. Liu, M. Liu, Z. Zhang, J. Zhang, Z. Tang, J. Li, Coarse-grained reduced $Mo_xTi_{1-x}Nb_2O_{7+y}$ anodes for

high-rate lithium-ion batteries. Energy Storage Mater. 34 (2021) 574–581. [DOI:10.1016/j.ensm.2020.10.016]

[S44] P. Jing, K. Liu, L. Soule, J. Wang, T. Li, B. Zhao, M. Liu, Engineering the architecture and oxygen deficiency of T-Nb_2O_5-carbon-graphene composite for high-rate lithium-ion batteries. Nano Energy 89 (2021) 106398. [DOI:10.1016/j.nanoen.2021.106398]

[S45] T. Li, G. Nam, K. Liu, J. Wang, B. Zhao, Y. Ding, L. Soule, M. Avdeev, Z. Liu, W. Zhang, T. Yuan, P. Jing, M. Kim, Y. Song, M. Liu, A niobium oxide with a shear structure and planar defects for high-power lithium ion batteries. Energy Environ. Sci. 15 (2022) 254–264. [DOI:10.1039/d1ee02664j]

[S46] Y. Yang, H. Zhu, J. Xiao, H. Geng, Y. Zhang, J. Zhao, G. Li, X. Wang, C. Li, Q. Liu, Achieving ultrahigh-rate and high-safety Li^+ storage based on interconnected tunnel structure in micro-size niobium tungsten oxides. Adv. Mater. 12 (2020) 1905295. [DOI: 10.1002/adma.201905295]

[S47] Q. Tian, W. Ye, X. Yu, H. Cheng, N. Zhu, M. Long, M. Shui, J. Shu, $WNb_{60}O_{153}$: A novel energy storage material with high rate capability. Ceram. Int. 2 (2019) 1893–1899. [DOI:10.1016/j.ceramint.2018.10.081]

[S48] W. Wu, M. Liu, Y. Pei, W. Li, W. Lin, Q. Huang, M. Wang, H. Yang, L. Deng, L. Yao, Z. Zheng, Unprecedented superhigh-sate and ultrastable anode for high-power battery via cationic disordering. Adv. Energy Mater. 12 (2022) 2201130. [DOI:10.1002/aenm.202201130]

[S49] M. Wang, Z. Yao, Q. Li, Y. Hu, X. Yin, A. Chen, X. Liu, J. Jiang, Y. Zhao, Fast and extensive intercalation chemistry in Wadsley-Roth phase based high-capacity electrodes. J. Energy Chem. 69 (2022) 601–611. [DOI:10.1016/j.jechem.2022.02.014]

[S50] Qian, H. Yu, L. Yan, H. Zhu, X. Cheng, Y. Xie, N. Long, M. Shui, J. Shu, High-rate long-life pored nanoribbon VNb_9O_{25} built by interconnected ultrafine nanoparticles as anode for lithium-ion batteries. ACS Appl. Mater. Interfaces 9 (2017) 30608–30616. [DOI: 10.1021/acsami.7b07460]

[S51] C. Lin, S. Yu, S. Wu, S. Lin, Z. Zhu, J. Li, L. Lu, $Ru_{0.01}Ti_{0.99}Nb_2O_7$ as an intercalation-type anode material with a large capacity and high-rate performance for lithium-ion batteries. J. Mater. Chem. A 3 (2015) 8627–8635. [DOI: 10.1039/c5ta01073j]

[S52] L. Hu, C. Lin, C. Wang, C. Yang, J. Li, Y. Chen, S. Lin, $TiNb_2O_7$ nanorods as a novel anode material for secondary lithium-ion batteries. Funct. Mater. Lett. 9 (2016) 1642004. [DOI: 10.1142/s1793604716420042]

[S53] L. Hu, R. Lu, L. Tang, R. Xia, C. Lin, Z. Luo, Y. Chen, J. Li, $TiCr_{0.5}Nb_{10.5}O_{29}$/CNTs nanocomposite as an advanced anode material for high-performance Li^+-ion storage. J. Alloys Compd. 732 (2018) 116–123. [DOI: 10.1016/j.jallcom.2017.10.145]

[S54] G. Liang, L. Yang, Q. Han, G. Chen, X. Liu, Y. Chen, L. Luo, Y. Li, C. Lin, R. Che, Conductive $Li_{3.08}Cr_{0.02}Si_{0.09}V_{0.9}O_4$ anode material: novel "zero-strain" characteristic and superior electrochemical Li^+-storage. Adv. Energy Mater. 10 (2020) 1904267. [DOI: 10.1002/aenm.201904267]

[S55] J. Zheng, R. Xia, C. Sun, N. Yaqoob, Q. Qiu, L. Zhong, Y. Li, P. Kaghazchi, K. Zhao, J. ten Elshof, M. Huijben, Fast and durable lithium storage enabled by tuning entropy in

Wadsley-Roth phase titanium niobium oxides. Small 19 (2023) 2301967 [DOI:10.1002/smll.202301967]

[S56] C. Lin, G. Wang, S. Lin, J. Li, L. Lu, $TiNb_6O_{17}$: a new electrode material for lithium-ion batteries. Chem. Commun. 51 (2015) 8970–8973. [DOI: 10.1039/c5cc01494h]

[S57] C. Yang, D. Ma, J. Yang, M. Manawan, T. Zhao, Y. Feng, J. Li, Z. Liu, Y. Zhang, R. Von Dreele, B. Toby, C. Albarrán, J. Pan, Crystallographic insight of reduced lattice volume expansion in mesoporous Cu^{2+}-doped $TiNb_2O_7$ microspheres during Li^+ insertion. Adv. Funct. Mater. 33 (2023) 2212854. [DOI:10.1002/adfm.202212854]

[S58] F. Wunde, F. Berkemeier, G. Schmitz, Lithium diffusion in sputter-deposited $Li_4Ti_5O_{12}$ thin films. J. Power Sources 215 (2012) 109–115. [DOI: 10.1016/j.jpowsour.2012.04.102]

[S59] C. Shi, K. Xiang, Y. Zhu, W. Zhou, X. Chen, H. Chen, Box-implanted Nb_2O_5 nanorods as superior anode materials in lithium ion batteries. Ceram. Int. 43 (2017) 12388–12395. [DOI: 10.1016/j.ceramint.2017.06.105]

[S60] W. Wang, J. Park, V. Nguyen, E. Jin, H. Gu, Hierarchical mesoporous rutile TiO_2/C composite nanospheres as lithium-ion battery anode materials. Ceram. Int. 42 (2016) 598–606. [DOI: 10.1016/j.ceramint.2015.08.153]

[S61] S. Schweidler, L. Biasi, A. Schiele, P. Hartmann, T. Brezesinski, J. Janek, Volume changes of graphite anodes revisited: a combined *operando* X-ray diffraction and *in situ* pressure analysis study. J. Phys. Chem. C 122 (2018) 8829–8835. [DOI: 10.1021/acs.jpcc.8b01873]

[S62] R. Li, G. Liang, X. Zhu, Q. Fu, Y. Chen, L. Luo, C. Lin, $Mo_3Nb_{14}O_{44}$: a new Li^+ container for high-performance electrochemical energy storage. Energy Environ. Mater. 4 (2021) 65–71. [DOI:10.1002/eem2.12098]

[S63] H. Yu, X. Cheng, H. Zhu, R. Zheng, T. Liu, J. Zhang, M. Shui, Y. Xie, J. Shu, Deep insights into kinetics and structural evolution of nitrogen-doped carbon coated $TiNb_{24}O_{62}$ nanowires as high-performance lithium container. Nano Energy 54 (2018) 227–237. [DOI: 10.1016/j.nanoen.2018.10.025]

[S64] S. Qian, H. Yu, L. Yan, H. Zhu, X. Cheng, Y. Xie, N. Long, M. Shui, J. Shu, High-rate long-life pored nanoribbon VNb_9O_{25} built by interconnected ultrafine nanoparticles as anode for lithium-ion batteries. ACS Appl. Mater. Interfaces 9 (2017) 30608–30616. [DOI: 10.1021/acsami.7b07460]

[S65] X. Zhu, H. Cao, R. Li, Q. Fu, G. Liang, Y. Chen, L. Luo, C. Lin, X. Zhao, Zinc niobate materials: crystal structures, energy-storage capabilities and working mechanisms. J. Mater. Chem. A 7 (2019) 25537–25547. [DOI: 10.1039/c9ta07818e]